Journal of Materials Chemistry A

Accepted Manuscript

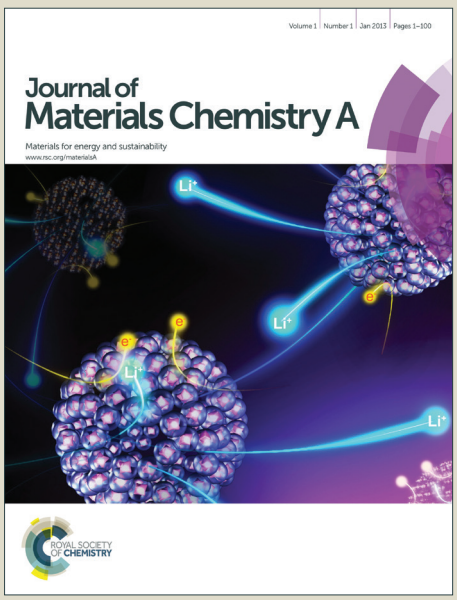

ROYAL SOCIETY OF CHEMISTRY

www.rsc.org/materialsA

High capacity silicon nitride-based composite anode for lithium ion batteries

Rhet C. de Guzman [a], Jinho Yang [b], Mark Ming-Cheng Cheng [b], Steven O. Salley [a] and K. Y. Simon Ng [a,*]

[a] Department of Chemical Engineering and Materials Science, Wayne State University, Detroit, MI 48202

[b] Department of Electrical and Computer Engineering, Wayne State University, Detroit, MI 48202

* Corresponding author. Tel.: +1 313 577 3805; fax: +1 313 577 8171.

E-mail address: sng@wayne.edu (K. Y. Simon Ng).

Abstract

A new composite material comprised of Si nitride (SiNx) derived from Si nanoparticles (SiNPs) via vacuum CVD approach, within a graphene matrix was synthesized as a potential Li ion battery (LIB) anode material. The deposition technique generated an external composition of Si_3N_4 and $SiN_{0.73}$ on the SiNP, with the overall N-levels increasing with deposition time. The SiNx electrochemical reaction can be attributed to a two-stage reversible mechanism: first the SiNx phase was converted to a matrix of Li_3N with embedded nano Si, then the Si content participates in the high capacity alloying/dealloying reactions. Galvanostatic cycling of the composite (50% Si w/w) using 500 mA g^{-1} displayed exceptionally stable capacity around 1400 mAh g^{-1} attributed to the improved stress management and conductivity of the Li_3N matrix. SiNx is demonstrated to be a compelling anode for LIB, with further development and optimization this might become the leading contender for the high capacity anode to possibly succeed current graphitic electrodes.

Introduction

An increasing variety of applications such as portable electronics and electric vehicles have increased the demands for improved commercial LIB capacity. New electrode materials are needed that can dramatically increase the battery's energy capacity. For anodes, the most promising candidate to substitute for the present electrode, graphite (theoretical capacity of 372 mAh g^{-1} [1]), is Si (theoretical capacity of 3,572 mAh g^{-1} [2]). With this switch, Li intercalation reaction with graphite (LiC_6) is replaced with an alloying reaction with Si producing a Li-rich phase ($Li_{15}Si_4$) that is capable of as much as ten-fold capacity increase. Unfortunately, during charge-discharge cycles, large volume variations in the Si-based anode (as much as 370 %) and stress on the bulk matrix are induced, ultimately leading to the anode's failure.

As a response, various strategic schemes have been pursued to alleviate the effect of volume expansion, including amorphous thin films [3-6], nanowires [7-9], nanotubes [10], and other porous morphologies [11-13]. While improvements in capacity have been achieved, cycle life and capacity degradation are still a concern. Recent advances are focusing on 3D nanostructured architecture [14-16] due to the improved Li^+ transport path, increased surface area and better volume-stress management during electrochemical cycling. Composite anodes employing SiNP coupled with carbonaceous material[15, 17-24] as a form of support have recently demonstrated the most promise; however, there is still room for further innovation.

A matrix comprised of chemically exfoliated graphene sheets is employed in this study due to its great potential as a support material. The highly organized sp^2-bonded C atoms in graphene provide outstanding mechanical and electrical properties compared with other known materials [25, 26]. It has the potential to assist in the electron conductivity in composite anodes while providing a matrix for the SiNPs. Being the building layers of graphite and similar with C-

based morphologies used in batteries, it also has excellent chemical stability that is crucial in minimizing intensive side reactions between the SiNPs and the electrolyte which forms a nonconducting solid-electrolyte interphase (SEI) [17] which irreversibly consumes Li during formation and bars Li^+ diffusion which ultimately degrades electrochemical performance.

Nano-sized Si particles benefit from having high surface area: increasing sites for Li alloying to improve electrode capacity. However, this attribute also gives rise to intensive side reactions with the electrolyte (especially $LiPF_6$ species) as reported by Aurbach et al.[27] forming unstable SEI. Also, since the Li-rich alloying reactions are still the governing reactions with Si-based anode materials, full mitigation of the cycling volume expansion is very difficult to accomplish. Due to this, even though SiNPs have high surface-to-volume ratio increasing the fracture toughness [28], volume variations are still considerable. Even for particles within the nanometer range, volume expansion (much worse fracturing) of particles due to cycling could lead to successive cycles of SEI rupture and reformation that will lead to further irreversible loss of Li (and capacity). In response to this inherent problem, we are proposing a novel SiNx-based composite anode that utilizes the conversion reaction pathway to divert from full Si alloying reaction (and its detriments). Battery conversion reactions follow a general scheme [29] (Eq. 1) in which an active electrode material, MA_x (A being an anion), reacts with Li to form its reduced state as a nanomaterial, M, as well as a Li-based compound matrix material. In the specific case of SiNx anodes, a two-stage reaction is expected to occur: the conversion reaction (Eq. 2), followed by the traditional alloying of the resulting SiNP (Eq. 3).

$$M^{Z+}A_x + ZLi \overset{cycles}{\Longleftrightarrow} M^0 + xLi_{Z/x}A \qquad (1)$$

$$SiN_x + ZLi \overset{cycles}{\Longleftrightarrow} Si^0 + xLi_{Z/x}N \qquad (2)$$

$$Si^0 + xLi \overset{cycles}{\Longleftrightarrow} Li_xSi \qquad (3)$$

The Li-N compound provides a matrix into which the nanomaterial particles can embed. The matrix is expected to act as a buffer region for the stress resulting from the large volumetric variation brought by the Si alloying reactions. SiNx synthesized using a facile nitriding process of SiNP, and prepared as a composite anode with graphene via a surfactant-assisted particle dispersion procedure is investigated in this study. The reaction mechanisms (and products) are elucidated through electrochemical, imaging and spectroscopic investigations. The resulting improvements brought by this novel chemistry will promote SiNx as a promising material contributing to the further advancement of SiNP-based composite anode and the LIB anode in general.

Experimental procedures

Graphite oxide synthesis

Graphite oxide was prepared using a modified (two-stage) Hummers' method [30]. In stage one, graphite (2 g, Dixon Microfyne, Ashbury, NJ) was pre-oxidized in an oil bath at 80°C for 4.5 h using 30 mL H_2SO_4 (95%) with pre-dissolved $K_2S_2O_8$ (1 g) and P_2O_5 (1 g). After cooling, the solution was diluted with 1 L of deionized water (DI), and then filtered and washed until the filtrate was pH neutral. Stage two follows the Hummers' method. The pre-oxidized graphite was mixed with 80 mL H_2SO_4 in an ice bath. While maintaining stirring, $KMnO_4$ (10 g) was added at slow increments for the reaction to proceed just below room temperature for 2 h then followed by careful dilution using 150 mL DI. During this process, the solution temperature was kept below 50 °C. After additional stirring for 2 h, further dilution with 500 mL DI was then followed by slow addition of H_2O_2 (30 %, 8.3 mL). The mixture was then allowed to settle overnight and then decanted. The product was purified using repeated rinsing and centrifugation with 5% HCl.

The graphite oxide was further washed with DI until pH neutral, then DI was added resulting in a graphite oxide suspension concentration of about 10 mg mL^{-1}. It was then stored in an amber bottle at room temperature.

Nitriding of SiNPs

SiNPs (polycrystalline) from Meliorum Nanotechnology (5-10 nm, Rochester, NY), previously stored in an Ar-filled glovebox with O_2 and moisture content both <1 ppm, were transferred inside the vacuum CVD chamber (Lindberg Blue M 55346, Watertown, WI). Utmost care was observed to prevent any contamination during handling. The system was purged with a stream of N_2 for 1 h before heating. Then, anhydrous ammonia feed (120 mL min^{-1}) was used to introduce nitrides to the target. The reaction temperature was 950 °C with different exposure times (0.5 h, 1 h, and 2 h) creating varying N-levels on SiNP resulting in SiNxNP. After the deposition, the particles were stored back to the glovebox to prevent any unwanted reactions with the room ambient atmosphere.

Composite anode formation

SiNxNP were first dispersed in methanol and sonic probed (Misonix, Ultrasonic Cell Disruptor, Farmingdale, NY, 100W, 22.5 kHz) for 15 min; afterwards a 1% (v/v) content of n-octyl alcohol (99%) was added, then subjected to 45 min of additional sonication. After this dispersion step, the standalone composite anode was produced without the need for binders and conductive diluents following the procedures as outlined in Lee's work [15]. An appropriate amount of graphite oxide suspension was added to the SiNx dispersion to make a 1:1 weight ratio (Si:C).

Then it was sonicated for 2 h. Sonication exfoliates the expanded structure of graphite oxide to form the graphene oxide (GO) platelets while at the same time dispersing the particles. All sonication-based steps were performed at room temperature and were closely monitored to minimize temperature increase. After this, the sample was vacuum–filtered (setup: Millipore 47 mm all-glass vacuum filter holder – funnel and flask; filter: 0.2 μm pore, Whatman Anodisc) forming a solid composite. During filtration, particle cross over was minimized due to the initial deposition of GO platelets on the filter surface. The resulting composite was then air-dried overnight, and then thermally reduced to achieve the standalone SiNxNP/graphene composite material. Reduction was performed using 10% H_2 (balance Ar, 100 mL min^{-1}) at 700 °C for 1.25 h. After the thermal treatments, the composites were sampled, weighed and prepared for testing.

Battery assembly

The anode materials were loaded and assembled using a CR2032 button cell assembly. On average, ~0.5 mg of the composite (1.5 mg cm^{-2}, 5-10 μm thick) was used as the working electrode and Li metal (99.9%, 0.75 mm thick, Alfa-Aesar) acting as both counter and reference electrode (half-cell configuration). A pre-prepared solution of 1.0M $LiPF_6$ dissolved in 1:1 (v/v) ethylene carbonate (EC)/ dimethyl carbonate (DMC) from Novolyte technologies (Independence, OH) was used as the electrolyte. The cells were assembled and crimp sealed in an Ar-filled glovebox.

Characterizations

General characterizations

Field emission scanning electron microscopy (FESEM) images were taken using a JEOL Model JSM-7600F (Peabody, MA) at 15 kV. Chemical composition analysis was done using the equipped Energy Dispersive X-ray Spectrometer (EDX). X-ray photoelectron spectroscopy (XPS) analysis was conducted with a PHI 670 Scanning Auger Nanoprobe (Physical Electronics, Chanhassen, MN) at 220 W X-ray power. A survey scan was first initiated and then high resolution multiplexes on each element of interest with 23.5 eV pass energy was performed. Deconvolutions of target peaks were accomplished with the AugerScan (RBD Instruments, Bend, OR) software. Prior to any processing, the peaks were smoothed using Savitzky-Golay algorithm and then followed by a Shirley background subtraction. Line shape fits were achieved using symmetric Gaussian-Lorentz functions. Quantifications of atomic fractions and binding distributions were also obtained by means the software functionalities.

Electrochemical characterizations

Electrochemical cycling was performed galvanostatically with a cut-off voltage range of 0.035 – 1.3 V. Two formation cycles were performed initially at 100 mA g^{-1}, the rate performance of the cells was investigated using 500 mA g^{-1} for 40 cycles (after the formation steps), then varying densities of 900, 1500, and 2500 mA g^{-1} for every 10 cycles. The cells were then cycled back to a current density of 500 mA g^{-1} in order to measure the changes in capacity following previous high current density cycles. In another batch of runs, a constant current density of 500 mA g^{-1} was applied for 100 cycles to assess the cycle life. Cyclic voltammetry (CV) measurements were performed using a single scan rate of 0.04 mV s^{-1} over a range of 0.01 – 1.5 V to gain a better understanding of the reaction mechanisms. The baseline performance of the particles was evaluated using a composite anode containing pristine SiNP (without any

modifications). The electrochemical cycling tests were done using a Gamry (Warminster, PA) Reference 3000, Gamry series G 300 or a Maccor (Tulsa, OK) Series 4200 cycler. Electrochemical impedance spectroscopy (EIS) measurements were performed using a Parstat 2273 with an AC voltage amplitude of 5 mV in the frequency range of 0.1 to 100,000 Hz. All electrochemical tests were performed at room temperature and only after the open circuit potentials were stable.

Results and discussion

Graphene as a support material for the SiNPs has been demonstrated as an effective component of the composite anode by earlier works [31, 32]. The graphene matrix promotes stable electrochemical cycling, improves the composite's conduction network with the active particles, as well as contributes in the charge storage (minor) capability of the overall electrode.

After the CVD procedure, the deposition of nitrides on SiNP produced the SiN_xNPs. Figures 1a and 1b depict the representative clusters of SiNP and SiNxNP (2h), respectively. From the micrographs, the sizes of SiNxNP appear to be larger than its unmodified counterpart. Higher magnification of the particles (Fig. 1 insets) indicates that the nitrided particles have rougher topography giving some insight on the deposition technique. EDX compositional analyses, as well as more surface sensitive XPS measurements were both performed on the particles. Since the particles are typically around 50-100 nm in diameter, the EDX measurements (Fig. 2a) are treated as the bulk particle composition. As expected, the amount of N increased, to a maximum of ~7 %, with the increase in deposition time. With this addition, Si amount decreases, although still the main component of the particles. The increase of the O level after nitriding is likely the effect of the Si dilution. Closer analysis of the particles' surface using XPS

(Fig. 2b) revealed the effect of the CVD process. Since Si is very susceptible to surface oxidation, the initial SiNP is primarily composed of O and nearly at a 2:1 ratio with Si. The O 1s spectra (peak: 532.4 eV) verified that majority of the O bonding is with Si, forming SiO_2. With the introduction of nitrides on the particles, the amounts of O and N present an inverse relationship: O is decreasing while N is increasing with deposition duration. This possibly is a result of a simultaneous dual mechanism inside the CVD chamber. While the N from the NH_3 reaction gas deposits on the Si to form SiNx, the remaining H acts to reduce oxides, making the whole process a deposition and a reduction procedure. Si, on the other hand, appears to remain consistent. This and the higher O and N content (compared with Fig. 2a) clearly confirm that the deposition is mainly onto the surface of the particles. With this, the SiNx can be inferred as an external gradient of SiNP. Close up analysis of the Si 2p3/2 spectra (Fig. 3a) showcase three distinct peaks at 100.6, 101.8 and 103.9 eV, corresponding to the estimated compositions of $SiN_{0.73}$ (34.2 %), Si_3N_4 (40.5 %) and the expected SiO_2 (25.3%), respectively. In order to verify the SiNx products further, the high resolution spectra of N 1s (Fig. 3b) was similarly investigated. Peaks at 397.3 and 398.5 were the best fit for the data, which can be assigned to $SiN_{0.73}$ and Si_3N_4, respectively. From the N 1s spectra of all the three SiNx (with varying CVD reaction times) samples, the make-up of Si-N bonding were plotted (Fig. 3c). A linear change in the distribution of SiNx compounds was observed as the nitriding time is increased: increasing for $SiN_{0.73}$ and decreasing for Si_3N_4.

In order to elucidate the reactions in Eq. 2 and 3, Fig. 4a summarizes both composites' (SiNP/graphene and SiNxNP/graphene) first two charge (lithiation)-discharge (delithiation) potential profiles using 100 mA g^{-1}. Overall, the profiles indicate successful electrochemical reaction: plateau regions are highly evident beginning at 0.3 V during charge and at 0.5 V during

discharge. These potential ranges are characteristics of known Si alloying/dealloying reactions with Li [7, 10, 18, 19, 33]. During the SiNP/graphene first charge, at higher potentials, SEI-formation related features predominate. The interphase presents diminished ionic conductivity as well as irreversible consumption of Li, as a result, reduced discharges are observed with an efficiency of ~70%. With the SiNx, the potential immediately dives to just above 0.5 V, then followed by a linear slope to about 0.1 V. The drop is an observed trait in reactions requiring phase transformation (conversion) as with the expected formation of the Li-N compound. The linear slope is present due to the multi-stage reactions corresponding to the transformation of different states of SiNx to form the Li-N compound (and the Si nanomaterial). After these, a sharp elbow at 0.1 V follows with the typical alloying plateau, corresponding to Eq. 3, until the end of the charge process. For the discharge, the noticeable difference happens below 0.5 V. While the SiNP immediately approach dealloying potential (~0.5 V), SiNx proceeds steadily (linearly with low slope). This indicates that discharge at the Li-N sites is also occurring, performing reversible reactions.

The CV curves (Fig. 4b) of the composites corroborate the Si alloying/dealloying reaction potentials happening at two Si phases [34, 35]. For both composites the alloying peaks are observed at ~0.25 V and those in ≤ 0.1 V (diluted 0.05 V is attributed to the crystallization of the amorphous Li-Si phase brought by deep charging). During dealloying, two major peaks are evident within 0.3 – 0.5 V window. Previous examination of the SiNP/graphene anode [31] indicate that peak broadening is likely due to the inclusion of peaks from the charge storage contribution of the graphene matrix. Using SiNx/graphene, the peaks at both the anodic and cathodic branches are even more broadened, appearing as one, compared to the peaks of SiNP/graphene. This observation suggests that aside from the Li-Si charge-discharge reactions (and graphene

contribution), the Li-N compound is reversibly performing as an active material contributing to the overall electrochemical mechanism. Also, the voltammograms for SiNx composite are evidently noisy at the reaction potentials signifying substantial morphological transformations. With these and the SEI formation, SiNx was expected to have lower Coulombic efficiency. However this was not observed. The initial efficiency of SiNx is computed to be around 77%, higher than that of SiNP and other conversion anodes. This is likely attributable to the emergence of the Li-N compound: the main difference between the two composite materials. In order to further investigate this, detailed study of representative SiNx N 1s high resolution XPS spectra before and after cycling was performed (Fig. 5a). The pristine SiNx mainly show the two marked peaks for the binding configuration of $SiN_{0.73}$ and Si_3N_4 making up 47.7 % and 52.3 % of the binding contributions, respectively. After being exposed to electrochemical cycling with Li, a new peak appeared around 399.7 eV, quenching the original N 1s peak. This peak confirms the existence of Li_3N [36] as being the Li-N matrix compound resulting from the conversion reaction (Eq. 2). With its emergence, the new binding distributions are as follows: 17.8 % for $SiN_{0.73}$, 43.9 % for Si_3N_4 and 38.3 % for the Li_3N. This indicates that the formation of the Li_3N matrix primarily comes from the conversion of $SiN_{0.73}$. Li_3N has been well studied to have high ionic conductivity to around 2-4 x 10^{-4} S cm^{-1} and possibly beyond[37, 38]. It is presently a subject of intense study as a candidate solid electrolyte for LIB. In line with its conductivity, modeling studies explained that Li_3N permits the fast and efficient Li^+ transport through its crystal structure[38, 39]. EIS measurements for SiNP (Fig. 5b) and SiNxNP (Fig. 5c) composites likewise support this. Focusing on the semicircle part (charge transfer resistance) of the Nyquist plot (which also contains a sloped straight line pertaining to diffusion resistance through the bulk material), the resistance magnitudes through the number of cycles are much lower in SiNx. This

suggests the ease with which charges can go in and out of the SiNx structure during cycling to both react with Li_3N and the nano Si embedded on it. The EIS evidence can likewise imply that the SEI deposition on SiNxNP/graphene was suppressed compared with the SiNP/graphene. The potential profiles of the first charge of the composites in Fig. 4a support this finding.

The SiNx-based composites were also tested for cycling and rate performances and the results are displayed in Fig. 6a, in parallel with this, Fig 6b illustrates the transformations that occur on the anode materials as cycles are performed to better explain the observed performance. Cycles were able to be performed due to effectiveness of the graphene matrix as a means to connect the active particles via a 3D conducting network. During the first 2 cycles using 100 mA g^{-1}, the displayed discharge capacities were higher for anodes formulated to be 50% by weight Si. This is likely due to the high surface area of the active components coupled with low current density [15]. After forming/activating the anode materials, 40 cycles using 500 mA g^{-1} followed and demonstrated a very distinct cycling trend. While the SiNP-based anode performed as typical electrodes would perform, with high capacity for the initial cycles followed by a decreasing trend, the SiNx-based anodes displayed increasing capacity. The reactions of SiNP-based anode are known to be the alloying/dealloying reaction with Li, which yields the high capacity values observed during the cycles. However, the reactions also bring about the severe volume expansion of the particles and the unstable SEI formations leading to the stepwise decay in capacity. As observed, the SiNP discharge was initially around 2040 mAh g^{-1} and after 42 cycles retained about only 59% (1200 mAh g^{-1}) of the initial capacity.

In the case of the SiNx anodes, the conversion reaction appears to have a predominant effect on the cycling performance even at low N-content levels. At the first formation charge (Fig. 6b i-ii) following the path of Eq. 2 then Eq. 3, the original SiNx structure was converted to

the Li_3N matrix material bearing the nano-Si due to the ample rate. After this, the alloying reaction took place and lithiated both the embedded Si in the matrix on the particle external and the crystalline SiNP (c-Si) center creating amorphous Li_xSi (a-Li_xSi) sites. At the succeeding discharge (Fig. 6b iii), since the conversion reaction is reversible the lithiated sites at the exterior are delithiated and recovered back to a degree. Majority at the interior, the discharge of the a-Li_xSi phase creates the amorphous Si (a-Si) sites that are desirable for highly reversible cycles. The capacities are at maximal due to the relaxed rate that was applied. However, as soon as the current density was increased to 500 mA g^{-1}, the discharges were at lower capacity values: 1044, 954 and 490 mAh g^{-1} for 2 h, 1 h and 0.5 h, respectively. As a possible explanation, during the switch to higher current loading, the Li^+ going to the particles preferentially convert the SiNx exterior to Li_3N and produced the nano Si sites within the matrix as opposed to the deep alloying reaction of the particle interior resulting in Fig. 6b iv. This is because the conversion step is happening at the higher potential state (happening first during charging) than the Si lithiation. Likewise, the observed capacity fluctuations hint continuous structural transformations occurring on the charging/discharging sites. Since the Li^+ mainly went to the formation of the matrix, the succeeding discharge (Fig. 6b v) in the Si sites show lower overall capacity count as indicated by the Coulombic efficiencies. Since the charging program occurs until 0.035 V (< 0.170 V), as the cycles progress (Fig. 6b vi) with Li_3N as an ionic conductor, more alloying sites become available [34] for the faster charge. As a result, both cycling efficiencies and discharge capacities are observed to be increasing (as much as 1245 mAh g^{-1} for SiNx 2h at 42nd discharge). At this point the SiNx is at par with the SiNP even though starting at a lower value.

Further increasing the cycling rates (900-2500 mA g^{-1}) to assess the rate capabilities of the anodes produced a progressively lower discharge capacity for SiNP. At the highest rate, SiNP

discharge was ~450 mAh g^{-1}, about 38 % of the capacity at cycle 42. This is expected since higher rates present challenges for reaction kinetics for Si. For SiNx, however, higher capacity drops were observed. The best case was 30% (375 mAh g^{-1}) retention from SiNx at 2h as compared with its 42nd cycle. It is believed that a more limiting scenario similar to Fig. 6b iv-v is occurring, Coulombic efficiency drops during the start of each elevated rates (cycles 43, 53 and 63) which relate that the transformations present irreversible capacity losses. As the cycles are done, the high rates and primary conversion reactions would only allow shallow lithiation of the interior a-Si (Fig. 6b iv), resulting in a significantly lower discharge output. Compared to the directly available alloying sites of SiNP, strategic cycling preparations are needed for the SiNx exterior to be able to effectively host Li^+ at high rates of charge/discharge. Nonetheless, within the SiNxNP/graphene composite group, it is evident that the higher N-level the better the performance. This gives us an insight as to the possibility of an anode material with higher level of SiNx to be capable of improved performance once the transformations and high capacity Si reaction sites are available.

After performing the high rates, the current density was reduced back to 500 mA g^{-1} to assess the capacity decay brought by the stresses of fast cycling. Accounting for the capacity decay for the first 40 cycles, it appears that SiNP's cycle 70 is a continuation of its decay trend. No significant degradation was added to it due to the high rates. Interestingly, for the SiNx-based anodes the discharge values recovered even higher than at cycle 40. This may be attributed to the improvement that Li_3N imparts on the whole anode. Given that a-Si alloying sites are available, the matrix's high conductivity will permit the efficient travel of ions for improved performance. But as the cycles continue there is now an evident decline of capacity. Taking note that the cycling efficiencies are still > 99 %, the decay may be related to the typical failures in the Si sites

(similar to those in SiNP). A possibility is illustrated as Fig. 6b vii and viii, the transformational changes during high rates coupled with deep charging cycles that particles experienced resulted in the expected volume expansion that ultimately led to the rupture of the SiNx exterior. At this point, the rate of capacity degradation appears to be comparable with the plain SiNP (especially SiNx 0.5h). With the higher levels of nitriding, the Li_3N improvement seems to still be in effect, with slower decay as compared to the SiNP/graphene. As a positive note, all three SiNx composites are still performing better than the SiNP/graphene anode at this point.

Figure 6c reported the results of extended low rate cycles (500 mA g^{-1}) using new SiNx composites. Similar to what was observed in the early runs of Fig. 6a, this batch clearly showed that it begins at a lower point and as cycles progress and the necessary transformations occur, more Si sites are available for cycling and thus higher discharge values are achieved. This cycling trend also confirms that the decay on the latter part of Fig. 6a is likely induced during the high current density cycles. Continuing until 200 cycles, about 1400 mAh g^{-1} was observed for SiNx 2h with the capacity still displaying a stable behavior. Additionally, there is an observed improvement of performance with the increase of nitriding time similar to what was generally displayed in Fig. 6a.

In summary, the electrochemical reactions of using SiNx as an anode material were confirmed to be the conversion reaction followed by the Si alloying/dealloying reaction. At its present configuration, the SiNx-based composite anode presents stable electrochemical performance at 500 mA g^{-1} rate of cycling. Further optimization of the nitriding of SiNP to achieve higher N-content can potentially improve the high rate performance of the anode.

Conclusions

The use of a facile vacuum CVD technique can modify the SiNP surface to have an external gradient of SiNx. Two major Si-N configurations result from the procedure: $SiN_{0.73}$ and Si_3N_4. With the amount of N increasing with the deposition time, the amount of $SiN_{0.73}$ likewise follow this trend. During the conversion reaction, the SiNx exterior (mainly $SiN_{0.73}$) is converted to a matrix of high conductivity Li_3N into which the other nano Si products are embedded. Aside from the Si alloying/dealloying reactions, the Li_3N matrix also presents an active material that can participate in the electrochemical reaction. As the N-levels are increased in SiN_xNP/graphene, a stable capacity up to 1400 mAh g^{-1} is achieved. The predominant transformations happening on the anode structure restrains this conversion anode's rate capabilities through limitations of the Si alloying sites. Increase of the N-level as well as strategic formation cycles could potentially offer better high rate performance. With its present state, this SiNx conversion anode presents a promising material worthy of further studies.

Acknowledgements

Financial support from the Department of Energy (Grant DE-EE0002106) for this research is gratefully acknowledged.

References

1. J. M. Tarascon and M. Armand, *Nature*, 2001, 414, 359-367.
2. M. N. Obrovac and L. Christensen, *Electrochem Solid State Lett*, 2004, 7, A93-A96.
3. J. Graetz, C. C. Ahn, R. Yazami and B. Fultz, *Electrochem Solid State Lett*, 2003, 6, A194.
4. J. P. Maranchi, A. F. Hepp and P. N. Kumta, *Electrochem Solid State Lett*, 2003, 6, A198.
5. S. Bourderau, T. Brousse and D. M. Scheich, *J Power Sources*, 1999, 81-82, 233-236.
6. T. L. Kulova, A. M. Skundin, Y. V. Pleskov, E. I. Terukov and O. I. Kon'kov, *J. Electroanal. Chem.*, 2007, 600, 217-225.
7. C. K. Chan, H. Peng, G. Liu, K. McIlwrath, X. F. Zhang, R. A. Huggins and Y. Cui, *Nat Nanotechnol*, 2008, 3, 31-35.
8. C. K. Chan, R. Ruffo, S. S. Hong, R. A. Huggins and Y. Cui, *J Power Sources*, 2009, 189, 34-39.
9. K. Peng, J. Jie, W. Zhang and S. T. Lee, *Appl. Phys. Lett.*, 2008, 93, 0331051-0331053.
10. M. H. Park, M. G. Kim, J. Joo, K. Kim, J. Kim, S. Ahn, Y. Cui and J. Cho, *Nano Lett*, 2009, 9, 3844-3847.
11. H. Kim, B. Han, J. Choo and J. Cho, *Angew. Chem. Int. Ed.*, 2008, 47, 10151-10154.
12. H. C. Shin, J. A. Corno, J. L. Gole and M. Liu, *J. Power Sources*, 2005, 139, 314-320.
13. D. K. Kang, J. A. Corno, J. L. Gole and H. C. Shin, *J. Electrochem. Soc.*, 2008, 155, A276-A281.
14. S. A. Klankowski, R. A. Rojeski, B. A. Cruden, J. Liu, J. Wu and J. Li, *J Mater Chem A*, 2013, 1, 1055-1064.
15. J. K. Lee, K. B. Smith, C. M. Hayner and H. H. Kung, *Chem Comm*, 2010, 46, 2025-2027.
16. T. S. Arthur, D. J. Bates, N. Cirigliano, D. C. Johnson, P. Malati, J. M. Mosby, E. Perre, M. T. Rawis, A. L. Prieto and B. Dunn, *MRS Bull*, 2011, 36, 523-531.
17. H. Kim, M. Seo, M. H. Park and J. Cho, *Angew Chem*, 2010, 122, 2192-2195.
18. H. Xiang, K. Zhang, J. Y. Lee, C. Zou, X. Chen and J. Wu, *Carbon*, 2011, 49, 1787-1796.
19. S. L. Chou, J. Z. Wang, M. Choucair, H. K. Liu, J. A. Stride and S. X. Dou, *Electrochem. Comm.*, 2010, 12, 303-306.
20. N. Liu, H. Wu, M. T. McDowell, Y. Yao, C. Wang and Y. Cui, *Nano Lett*, 2012, 12, 3315-3321.
21. H. M. Jeong, S. Y. Lee, W. H. Shin, J. H. Kwon, A. Shakoor, T. H. Hwang, S. Y. Kim, B. S. Kong, J. S. Seo, Y. M. Lee, J. K. Kang and J. W. Choi, *RSC Adv*, 2012, 2, 4311-4317.
22. X. Zhou, Y. X. Yin, A. M. Cao, L. J. Wan and Y. G. Guo, *ACS Appl Mater Interfaces*, 2012, 4, 2824-2828.
23. T. H. Hwang, Y. M. Lee, B. S. Kong, J. K. Seo and J. W. Choi, *Nano Lett*, 2012, 12, 802-807.
24. B. S. Lee, S. B. Son, K. M. Park, J. H. Seo, S. H. Lee, I. S. Choi, K. H. Oh and W. R. Yu, *J Power Sources*, 2012, 206, 267-273.
25. Y. Hernandez, V. Nicolosi, M. Lotya, F. M. Blighe, Z. Sun, S. De, I. T. McGovern, B. Holland, M. Byrne, Y. K. Gun'Ko, J. J. Boland, P. Niraj, G. Duesberg, S. Krishnamurthy, R. Goodhue, J. Hutchison, V. Scardaci, A. C. Ferrari and J. N. Coleman, *Nat. Nanotechnol.*, 2008, 3, 563-568.
26. F. Banhart and P. M. Ajayan, *Nature*, 1996, 382, 433.
27. D. Aurbach, A. Nimberger, B. Markovsky, E. Levi, E. Sominski and A. Gedanken, *Chem Mater*, 2002, 14, 4155-4163.
28. M. H. Park, K. Kim, J. Kim and J. Cho, *Adv. Mater.*, 2010, 22, 415-418.
29. R. Malini, U. Uma, T. Sheela, M. Ganesan and N. G. Renganathan, *Ionics*, 2009, 15, 301-307.
30. N. I. Kovtyukhova, P. J. Ollivier, B. R. Martin, T. E. Mallouk, S. A. Chizhik, E. V. Buzaneva and A. D. Gorchinskiy, *Chem Mater*, 1999, 11, 771-778.
31. R. C. deGuzman, J. Yang, M. M. C. Cheng, S. O. Salley and K. Y. S. Ng, *J Mater Sci*, 2013, 48, 4823-4833.
32. R. C. deGuzman, J. Yang, M. M. C. Cheng, S. O. Salley and K. Y. S. Ng, *J Power Sources*, 2014, 246, 335-345.

33. U. Kasavajjula, C. Wang and A. J. Appleby, *J. Power Sources*, 2007, 163, 1003-1039.
34. M. N. Obrovac and L. J. Krause, *J Electrochem Soc*, 2007, 154, A103-A108.
35. Y. Fan, K. Huang, Q. Zhang, Q. Xiao, X. Wang and X. Chen, *J Mater Chem*, 2012, 22, 20870-20873.
36. Z. W. Fu, Y. Wang, X. L. Yue, S. L. Zhao and Q. Z. Qin, *J Phys Chem B*, 2004, 108, 2236-2244.
37. T. Lapp, S. Skaarup and A. Hooper, *Solid State Ionics*, 1983, 11, 97-103.
38. W. Li, G. Wu, C. M. Araujo, R. H. Scheicher, A. Blomqvist, R. Ahuja, Z. Xiong, Y. Feng and P. Chen, *Energy Environ Sci*, 2010, 3, 1524-1530.
39. K. Kowada, M. Tatsumisago and T. Minami, *Solid State Ionics*, 2009, 180, 462-466.

List of Figure Captions:

Fig. 1 Representative FESEM micrographs of the (a) SiNP and (b) SiNx clusters. Insets: Close examination of the particles' surface morphology. Scale bars are all 100 nm.

Fig. 2 Atomic concentrations of the particles subjected to different nitriding times using (a) EDX for bulk analysis and (b) XPS for surface characterization.

Fig. 3 High resolution XPS spectra of (a) Si 2p3/2 and (b) N 1s verifying the bonding configurations of between Si and N. (c) The linear dependence of the amount of $SiN_{0.73}$ and Si_3N_4 with respect to the nitriding time.

Fig. 4 (a) Charge-discharge profile of SiNP/graphene and SiNxNP/graphene composites during the first two cycles. (b) CV comparison of the two composites showing the pertinent reaction peaks.

Fig. 5 (a) High resolution XPS spectra for N 1s of SiNxNP/graphene anode before and after electrochemical cycles. Nyquist plots of (b) SiNP and (c) SiNx after the first 10 cycles focusing mainly on the charge transfer resistance.

Fig. 6 Cycling performance of both SiNP and SiNx-based composite anodes using (a) variable cycle runs ((b) proposed scheme of the SiNx/SiNP transformations during cycling, composition/interphase boundaries are exaggerated, not to scale) and (c) constant low current density (500 mA g^{-1}) cycle runs.

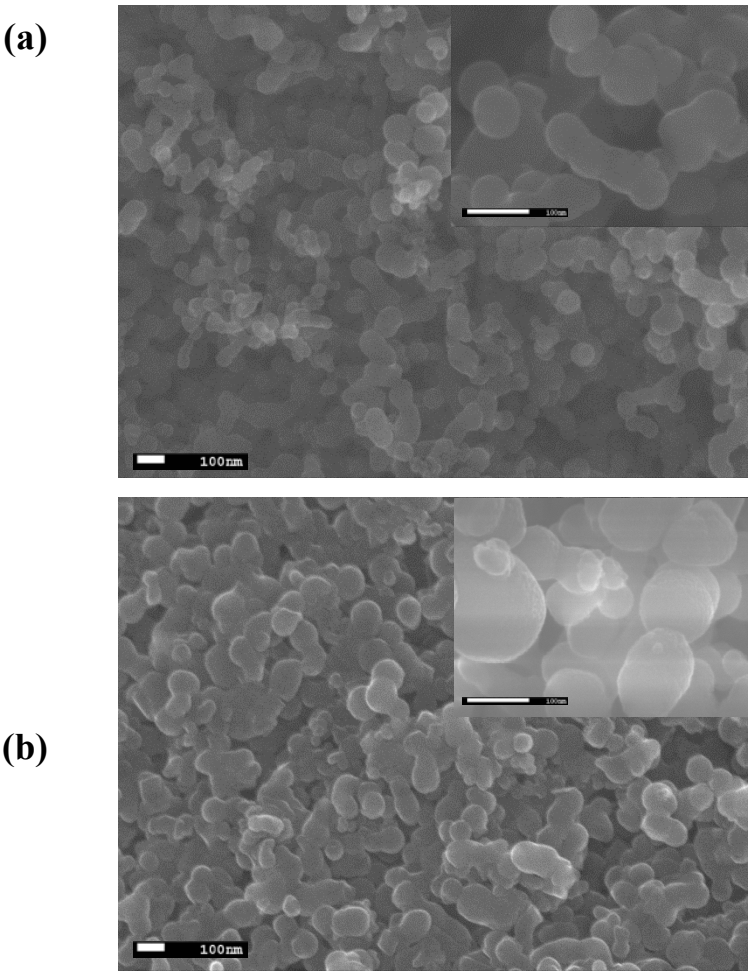

Figure 1.

(a)

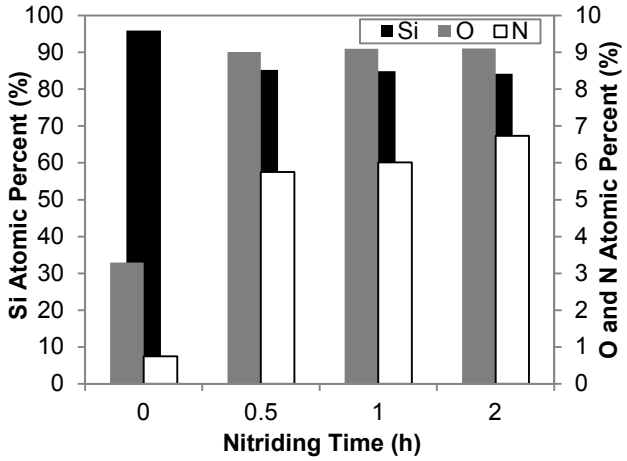

(b)

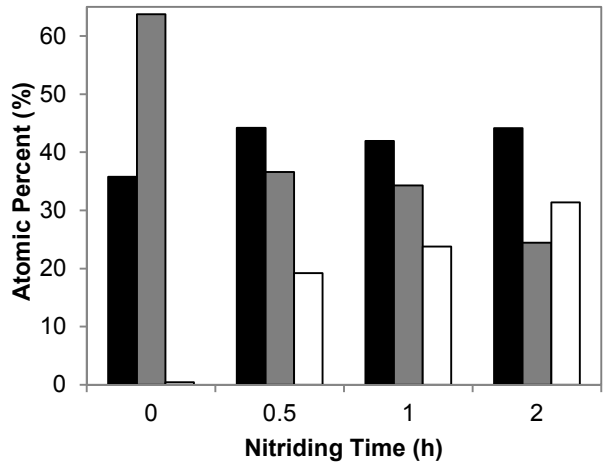

Figure 2.

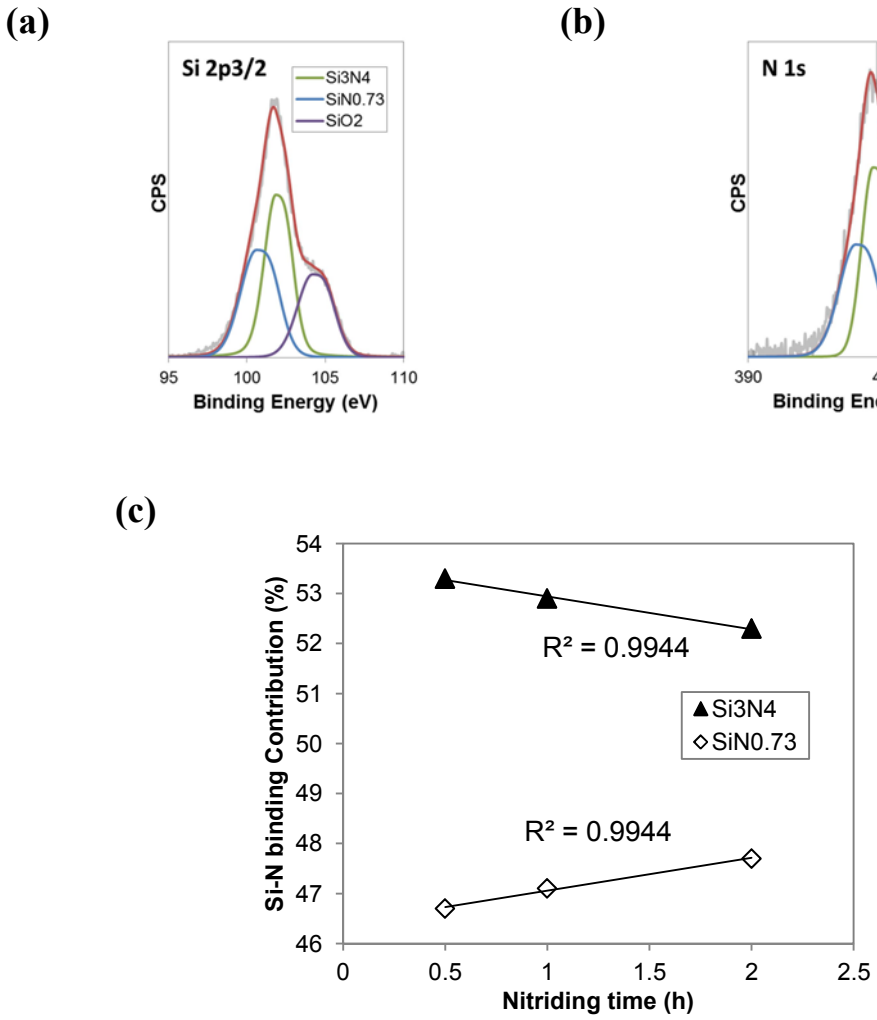

Figure 3.

(a)

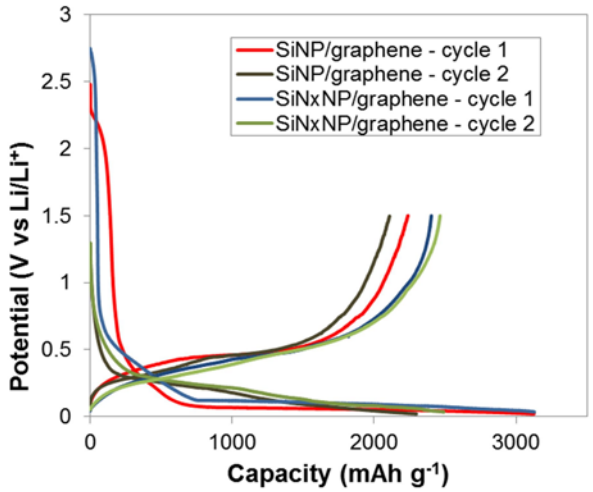

(b)

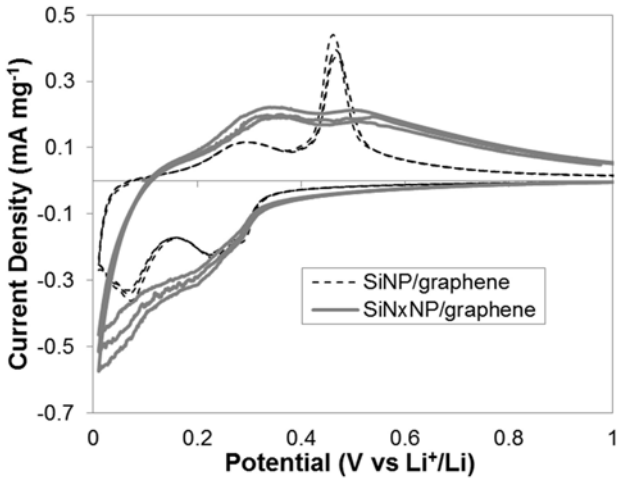

Figure 4.

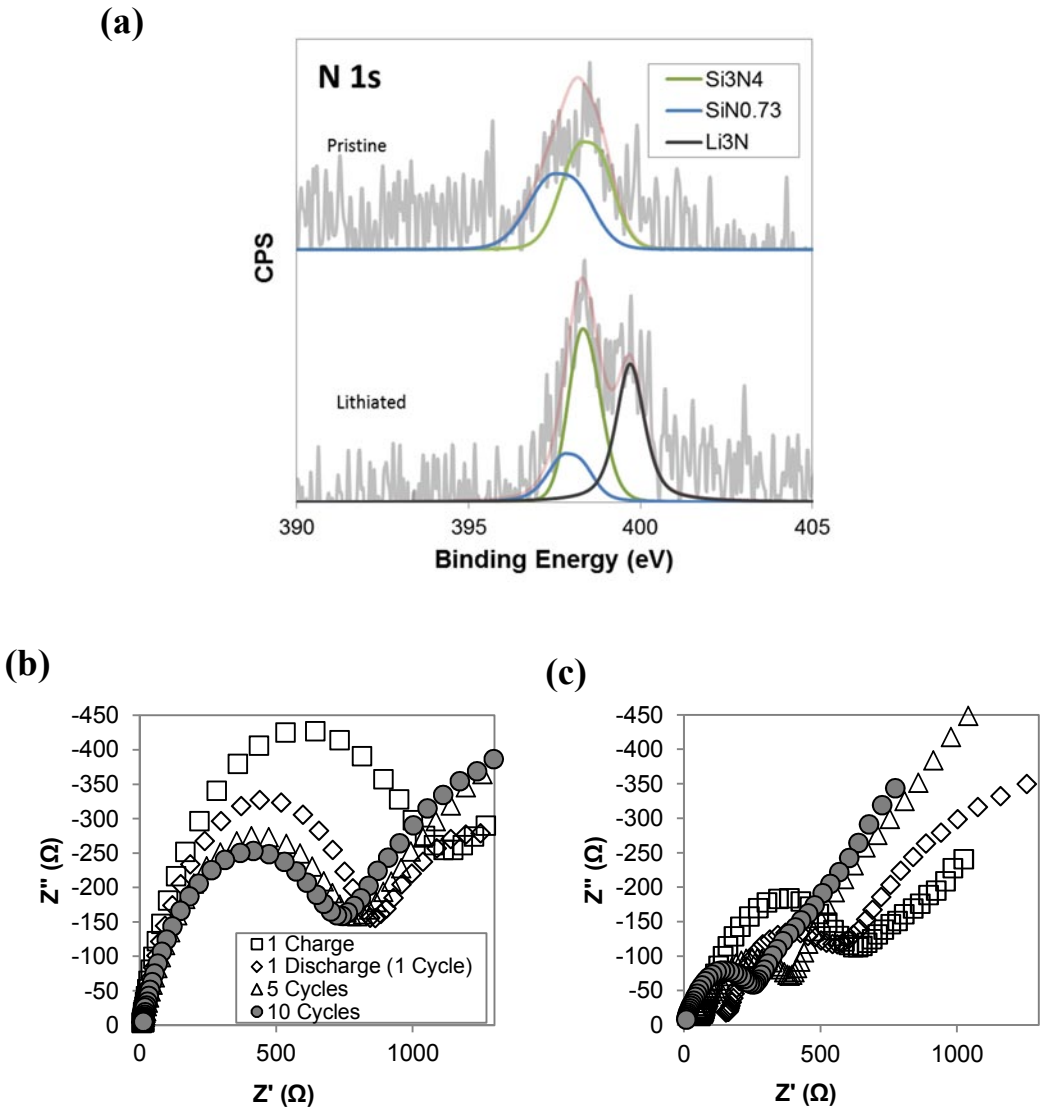

Figure 5.

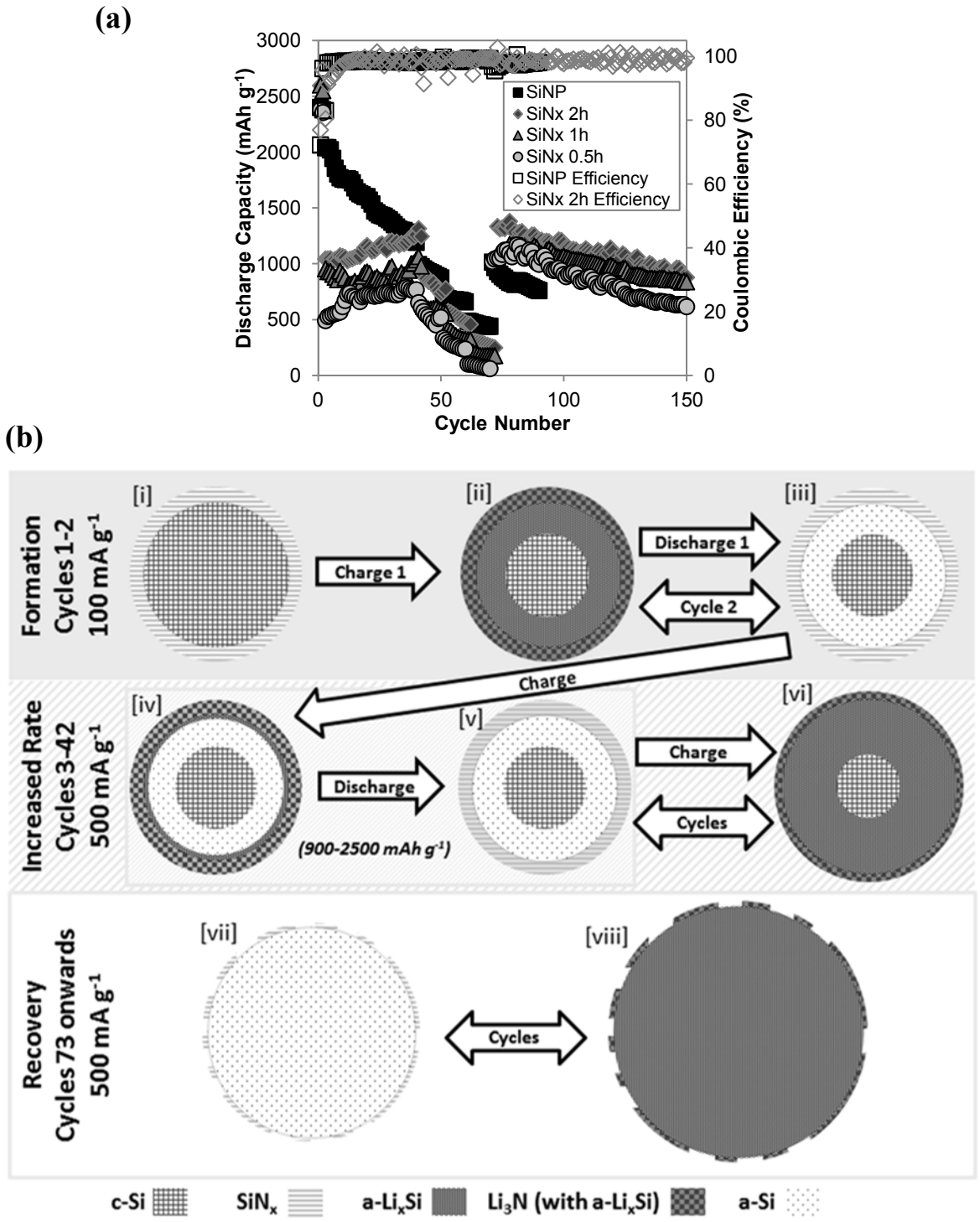

Figure 6.

(c)

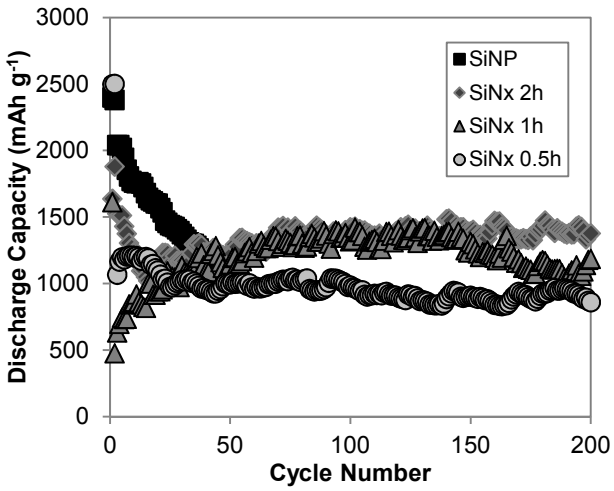

Figure 6.